Long-term corrosion behavior of FeCr(Al, Ni) alloys in O2 + H2O with KCl(s) at 600 °C: Microstructural evolution after breakaway oxidation

Corrosion Science 226 (2024) 111654

Contents lists available at ScienceDirect

Corrosion Science

journal homepage: www.elsevier.com/locate/corsci

Long-term corrosion behavior of FeCr(Al, Ni) alloys in O_2 + H_2O with KCl (s) at 600 °C: Microstructural evolution after breakaway oxidation

Vicent Ssenteza [a,*], Johan Eklund [a], Sedigheh Bigdeli [b], Torbjörn Jonsson [a]

[a] Chalmers University of Technology, Kemivägen 10, 412 96 Gothenburg, Sweden
[b] Höganäs AB, Bruksgatan 35, 263 39 Höganäs, Sweden

ARTICLE INFO

Keywords:
Alloy
EBSD
High temperature corrosion
Breakaway oxidation
Phase transformation

ABSTRACT

The microstructural evolution of the oxide scales formed on FeCr(Al,Ni) alloys after breakaway oxidation was studied in 5 % O_2 + 20 % H_2O + N_2 (Bal) + KCl(s)/KCl(g) at 600 °C for 168, 1000 and 8000 h. The SEM/EDS, SEM/EBSD and XRD investigation show that all alloys experience breakaway oxidation and form multi-layered scales. Experimental results, thermodynamic modelling and kinetic simulations show that FeCrAl and FeCrNi alloys form chromium-rich spinel oxide in inward-growing scales which transform into a protective corundum-type oxide as the oxidation progresses, while FeCr alloy experiences fast oxidation and maintains a non-protective spinel oxide/internal oxidation after long exposures.

1. Introduction

In order to develop and select materials for demanding corrosive high temperature applications such as biomass- and waste-fired boilers, the insight into the evolution of the oxide microstructure during long operation times in corrosive environments is very important. The combustion of biomass and waste is known to release flue gas that contains alkali salts, e.g., KCl, which accelerate the corrosion of superheater materials [1–16]. This may lead to lower efficiency of the power plant, i.e., through lower steam temperature, or to shorter lifetime of key components. In the boiler environments, the Cr-rich scale normally formed on a stainless steel, i.e., the primary protection, is quickly broken resulting in breakaway oxidation [9]. The scale formed after breakaway oxidation is known to be fast-growing and less protective consisting of an outward- and inward-growing part, i.e., defined as the secondary protection. The concept of secondary corrosion protection has been used in previous work to denote the corrosion regime after breakaway oxidation, see e.g., [17,18]. In the secondary corrosion regime, alloys may re-form a slow-growing and protective oxide layer, a.k.a a healing layer, at the metal/scale interface, which is rich in Cr and/or Al [8,17,19–21].

The protectiveness of the secondary protection is determined by several factors such as spallation or vulnerability towards corrosive species, e.g., Cl, but also on its ability to slow down ion diffusion through the oxide scale. This is known to be influenced by the oxide's grain size and the amount of alloying elements [17]. However, the key feature to form a good secondary protection, with healing layer characteristics, may be the ability to form a protective Cr/Al – rich scale in the metal/oxide interface. The formation of such a scale is determined by the access to Cr/Al, i.e., diffusivity/activity of these elements in the alloy as well as the inward diffusion of oxygen ions which determines the oxidation rate. Kim et al. [22] reported faster outward diffusion of Cr in a fine-grained alloy which led to formation of a protective Cr-rich oxide scale while the coarse-grained alloy formed less protective scale. Eklund et al. [23] showed that FeCr alloys with Cr-content of 2.25–18 wt% and FeCrAl alloys with < 18 wt% Cr and < 3 wt% Al exhibit corrosion behavior similar to pure iron after breakaway oxidation. Col et al. [20] investigated the microstructural evolution of Fe–18Cr–8Ni austenitic stainless steel at 850 °C in O_2 and reported the formation of a continuous Cr_2O_3 healing layer close to the metal/scale interface. While these previous studies provide insight into the microstructural features of scales formed after breakaway oxidation, the investigations are typically carried out for short-term exposures while the materials used in these types of applications tend to have operating lifetimes of several years. It is therefore very important to investigate long-term exposures where it is possible to assess the microstructural evolution and the protectiveness of the oxide scales formed on alloys exposed in harsh environments.

This investigation covers the long-term corrosion behavior of stainless steels and FeCrAl alloys at 600 °C exposed in harsh environments. The focus of the study is to investigate the microstructural evolution of

* Corresponding author.
E-mail address: ssenteza@chalmers.se (V. Ssenteza).

https://doi.org/10.1016/j.corsci.2023.111654
Received 4 May 2023; Received in revised form 30 October 2023; Accepted 4 November 2023
Available online 10 November 2023

the oxide scales during long-term exposures. The exposures were carried out in 5 % O_2 + 20 % H_2O + N_2 (Bal) + KCl(s)/KCl(g) at 600 °C for 168, 1000 and 8000 h in a setup where KCl(s) is active for all durations. The corrosion products were characterized using XRD and advanced electron and ion microscopy such as, SEM/EDX and EBSD on cross-sections prepared using Broad Ion Beam (BIB) milling. Thermodynamic calculations were used to predict oxide phases and compare with data obtained from the experimental investigation and kinetic-based simulations were performed to model the kinetics of key features of microstructural evolution.

2. Experimental procedure

2.1. Material preparation and exposures

Materials used in this study were SVM12 (martensitic stainless steel) supplied by Vallourec S.A, APMT (FeCrAl alloy) supplied by Kanthal AB and alloy 27Cr33Ni3Mo (Austenitic stainless steel) supplied by Alleima AB. The chemical composition of these alloys is presented in Table 1. The materials used in this study are candidate superheater materials. SVM12 exhibits excellent mechanical properties such as high creep strength [24], which is desirable for load bearing capability of the superheater tubes and can thus be used as substrate for coatings with good corrosion properties. The other two materials, APMT and Alloy 27Cr33Ni3Mo contain high chromium content which is known to be beneficial for the corrosion resistance of the alloy.

All the materials were received as coupons with dimensions of 20 mm × 10 mm × 2 mm. The coupons were ground with P500 and P800 SiC paper using a polishing machine. The ground samples were cleaned with acetone in ultra-sonic agitation bath and finally cleaned with ethanol. The investigated alloys were weighed using Sartorius™ scale with six decimal accuracies. The samples were sprayed with 2 mg/cm^2 KCl solution (consisting of KCl salt dissolved in 80 vol% ethanol with 20 vol% distilled water). During spraying, warm air was continuously passed over the samples to speed up the drying process of the solution. The samples were then kept in a desiccator for 24 h prior to exposure.

The corrosion test was performed isothermally in a three-zone horizontal silica tube furnace with a set temperature of 600 °C ± 3 °C in all the heating zones. The exposures were performed for 168 h, 1000 h, and 8000 h in an environment consisting of 5 % O_2 + 20 % H_2O + N_2 (Bal) (gas flow of 0.1 cm/s) with a KCl(s) source upstream. A complete description of the experimental setup can be found elsewhere [25].

2.2. Analysis

Prior to samples analysis, cross-sections were prepared by cutting the samples using a Leica EM TXP and milling the cross-sections using a Gatan PECS II broad ion beam (BIB) milling system (operated at 6, 4 and 2 kV for 2 h at each accelerating voltage). The samples were then analyzed using scanning electron microscopy (SEM) and energy dispersive X-ray (EDX) operated at an accelerating voltage of 10–20 kV with an FEI Quanta 200 in high vacuum mode. For XRD analysis, a Bruker D8 Discover was used with a Mo radiation source to ensure deep penetration through the thick oxide scales. Furthermore, phase identification was performed using Electron Backscattered Diffraction (EBSD) on a TESCAN GAIA3 dual beam instrument operated at 20 kV for all the analysis.

The average grain sizes for both the oxide and the steel were obtained from SEM-BSE cross-section images of milled samples using the intercept method described in the ASTM E112–12 standard [26]. In this method, a line is drawn across an area of interest and the total number of intersections between the line and the grain boundaries are recorded. Several lines were drawn to increase the number of intercepts and thereby increase the precision of the method.

2.3. Thermodynamic modelling and kinetic simulation

Thermo-Calc program (version 2023a) was used to calculate the amount of different phases formed under equilibrium to compare with the results obtained from the experimental investigations. Oxide database, TCOX12 was used for these calculations. In addition, diffusion-based simulations were run using Dictra module in Thermo-Calc and developed databases found here [27] to predict the oxide thickness after long-term exposures. Moving phase boundary model [28] was used in these simulations, in which the oxide growth is assumed to occur as a results of grain boundary diffusion in the oxide phase.

3. Results

The long-term high temperature corrosion behavior of SVM12, APMT and Alloy 27Cr33Ni3Mo was studied in laboratory conditions mimicking a simplified boiler environment consisting of 5 % O_2 + 20 % H_2O + N_2 (Bal) +KCl(s)/KCl(g) for 168 h, 1000 h and 8000 h. The amount of applied KCl(s), in combination with the low flow and an upstream KCl-filled boat, was calculated to last the entire duration of all exposures (up to 8000 h) [25]. The presence of KCl post exposure was confirmed for all samples through plan view SEM/EDX. It is worth noting that in contrast to boiler environment which contains many other corrosive species, the setup in this study is a simplified environment that offers well-controlled conditions for evaluating the corrosion behavior of studied materials.

3.1. Oxidation kinetics

The oxidation kinetics presented in this study are based on measured oxide thickness on the ion-milled SEM-BSE cross-section images for all the alloys under investigation. The oxide thickness measurement was chosen to represent the extent of the corrosion as it provides better certainty regarding oxide growth rate compared to mass gain measurement which could be misleading for samples exposed for long durations, especially if the samples were to suffer partial spallation during or after exposure. Through ion-milling, large cross-sections were obtained, and the oxide thickness measurements were performed from representative regions of the cross-sections. The spalled oxide could

Table 1
Chemical composition of alloys (wt%) used in this study.

Alloy	Chemical composition (wt%)										
	Ni	Cu	N	Fe	Cr	Al	Mo	Si	Mn	C	Others
SVM12	0.40		0.02	Bal.	10.50 - 12.00		0.10 - 0.60	0.20 - 0.60	0.30 - 0.80	0.10 - 0.16	W= 1.50–2.50 Co= 1.50–2.50 V= 0.15–0.30
APMT				Bal	20.50 - 23.50	5.00	3.00	0.70	0.40	0.08	RE
Alloy 27Cr33Ni3Mo	27.00 - 36.00	0.50 - 1.50	0.20	Bal.	25.00 - 31.00		3.00	0.80	2.00	0.10	RE

easily be identified when analyzing the oxide scale, i.e., by comparing the ratios between the outward/inward-growing oxides. Fig. 1 shows the calculated average oxide thickness and the spread in thickness is presented as error bars for the respective alloys and exposure times.

The results show that the alloys formed oxide scale thicknesses in micrometer range after the shortest exposure time (168 h) which is characteristic of the post-breakaway oxidation scales, confirming that the alloys have transitioned into the secondary corrosion mode in less than 168 h. This is in line with the results of previous studies investigating corrosion behavior of alloys of similar classes where it was reported that the protective scale is quickly broken down in environment containing KCl + water vapor leading to breakaway oxidation, see e.g., [15,17,20]. Under the present experimental conditions, the growth kinetics from 168 h therefore represent the oxidation kinetics in the secondary regime for the investigated alloys. SVM12 exhibited the fastest oxide growth rate after all the exposure times. Already after 168 h, SVM12 has formed a thick oxide (around 91 μm), indicating that the oxide growth is initially very fast growing for this alloy. After 8000 h-exposure, SVM12 had formed about 206 μm thick oxide. The data for oxide thickness and time was plotted in order to investigate the parabolic growth relationship ($x^{\alpha} = k_p t$), where x is the oxide thickness, α is the order of parabolicity, k_p is the parabolic rate constant and t is time. Numerically, $\alpha = 2$ denotes parabolic growth relationship and $\alpha > 2$ denotes sub-parabolic growth relationship. In this study SVM12 obtained $\alpha = 3.2$, which indicates that this alloy displays sub-parabolic oxide growth behavior.

In contrast, the measured thickness for Alloy 27Cr33Ni3Mo showed a slower-growing oxide scale after breakaway oxidation. After 168 h, the scale is 9 μm which increased to about 13 μm after 8000 h indicating slow oxidation kinetics in the secondary corrosion regime. APMT exhibited intermediate oxide growth rate where it formed a 25 μm thick scale after 168 h and twice as thick scale after 8000 h. Both APMT and Alloy 27Cr33Ni3Mo had calculated α values of 3.8 and 6.7 respectively, which indicate that these alloys exhibit sub-parabolic behavior with exposure time.

3.2. Microstructural investigation

The microstructure of oxide scales formed on SVM12, APMT and Alloy 27Cr33Ni3Mo was investigated in detail using SEM/EDS, XRD and SEM/EBSD for chemical analysis and phase identification as these features are a key input to growth kinetics as well as, e.g., oxidation simulations. Generally, the investigation showed that all the investigated alloys formed multi-layered oxide scales consisting of outward-growing and inward-growing layers. The interface between the outward- and inward-growing layers is interpreted as the original metal surface and is marked as dotted line in all SEM/BSE images. It is also worth noting that the compositions of oxides obtained from SEM/EDX analysis are presented as cationic concentration (at%) and that oxygen is excluded due to technical difficulty of quantifying lighter elements.

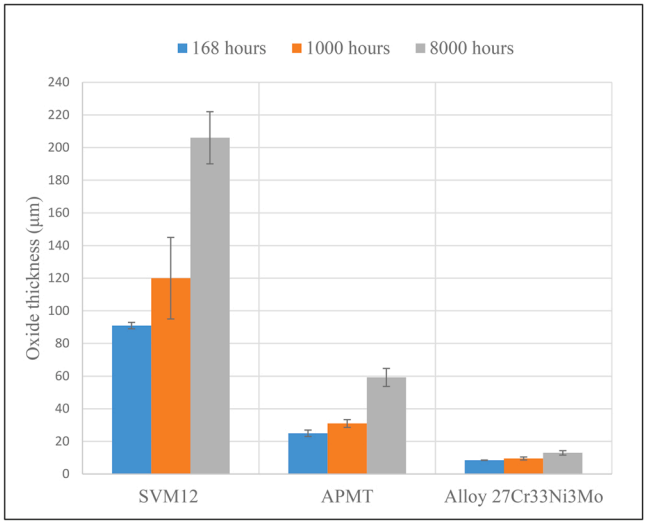

Fig. 1. Oxide thickness for the studied alloys after exposure in 5 % O_2 + 20 % H_2O + N_2 (Bal) + KCl(s)/KCl(g) for 168 h, 1000 h and 8000 h at 600 °C.

3.2.1. Martensitic stainless steel - SVM12

Fig. 2 shows a representative ion-milled SEM/BSE cross-section image of SVM12 after 168 h exposure (Fig. 2a), 1000 h exposure (Fig. 2b) and 8000 h exposure (Fig. 2c). The scales were all multilayered and the selected image regions show a representative variation in the thickness for different exposure times. The dashed lines indicate the interpreted interface between the inward- and outward-growing oxide layers.

After 168 h of exposure, SVM12 formed an approximately 91 μm thick oxide scale.

The scale is dense and contains K_2CrO_4 particles embedded in the outward-growing scale as identified by SEM/EDS elemental analysis. Further SEM/EDS and SEM/EBSD analyses revealed that the outward-growing layer consists of almost pure iron-oxide and consists of hematite in the upper regions (region I) and magnetite in the lower regions (region II), see indexed Kikuchi bands in Fig. 2a. The average oxide grain size in the outer scale was 1.5 μm. The inward-growing layer was identified as a spinel structure with a composition of 75 at% Fe and 25 at % Cr in region III and 60 at% Fe and 40 at% Cr in region IV. Further crystalline phase identification using XRD with Mo radiation source showed the presence of Fe_2O_3, Fe_3O_4 and Cr_2FeO_4 phases which is in good agreement with the EBSD results, see Table 2. Traces of Cl (less than 1-at%) were detected in the inward-growing scale while the outward-growing scale contained no indications of Cl. However, traces of K were detected in the outward-growing scale (apart from the K_2CrO_4 particles) but not in the inward-growing scale. The bright particles distributed within the inward-growing scale were identified as W-rich precipitates, which agrees well with observations made in these studies [29,30]. Beneath the scale, local chlorine-rich agglomerations were interpreted to be $FeCl_2$.

The ion milled cross-section on the sample exposed for 1000 h showed a similar microstructure as observed after 168 h exposure. The scale is slightly thicker (about 120 μm) and dense (Fig. 2b). In the oxide/gas interface, a continuous layer of large K_2CrO_4 particles is detached. According to SEM-EDS and SEM/EBSD analyses, the outward-growing layer consist of hematite in region I and magnetite in region II with average grain size of 2.4 μm. The inward-growing layer is indexed as spinel with an average composition of 70 at% Fe and 30 at% Cr in the upper regions (region III) and 55 at% Fe and 45 at% Cr in the lower regions (region IV). Traces of Cl (less than 1-at%) were again detected only in the inward-growing scale while traces of K were detected in the outward-growing scale.

After 8000 h of exposure, SVM12 forms a scale with the similar microstructure as after 168 and 1000 h. The scale is thicker and has an average thickness of approximately 206 μm (Fig. 2c) where all the layers (oxide phases) have become thicker. The outward-growing oxides (hematite and magnetite) contain small pores and large K_2CrO_4 particles are embedded in the inner regions (region II). The inward-growing oxide (again identified as spinel) is dense and homogenous closer to the original metal interface (region III) and porous in the lower regions (region IV). The average composition of these regions was 65 at% Fe, 35 at% Cr and 60 at% Fe, 40 at% Cr for regions III and IV respectively. W-rich precipitates (observed as bright particles in the SEM-BSE image (Fig. 2c)) in the inner region of the inward-growing scale have increased. Closer to the metal/scale interface, a 3 μm Cr-rich layer (65 at% Cr) has formed. No Cl was detected in the scale while traces of K were detected along the entire scale. Beneath the 3 μm thick Cr-rich layer, a14 μm deep Cr-depletion zone could be observed.

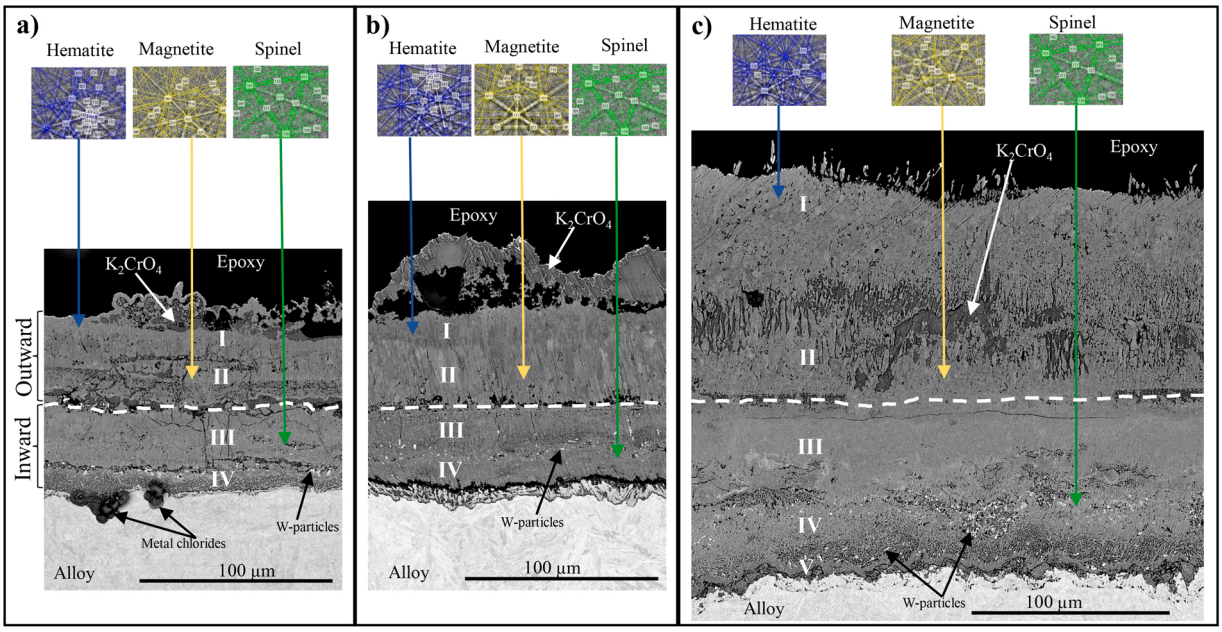

Fig. 2. SEM-BSE cross-section images of SVM12 after exposure for a) 168 h, b) 1000 h and c) 8000 h in 5 % O_2 + 20 % H_2O + N_2 (Bal) + KCl(s)/KCl(g) at 600 °C.

Table 2
Crystalline oxide phases identified using XRD.

Exposure (hours)	SVM12	APMT	Alloy 27Cr33Ni3Mo
168	BCC; Fe_2O_3; Fe_3O_4; $FeCr_2O_4$	BCC; Fe_2O_3; Fe_3O_4; $FeCr_2O_4$; $FeCrO_3$ $(Al_{0.9}Cr_{0.1})_2O_3$	FCC;Fe_3O_4; $FeCr_2O_4$; Fe_2NiO_4; $FeNiCrO_4$; $Cr_{1.3}Fe_{0.7}O_3$
1000	BCC; Fe_2O_3; Fe_3O_4; $FeCr_2O_4$	BCC; Fe_2O_3; Fe_3O_4; $Al_{1.82}Cr_{0.12}O_3$; Cr_2O_3	FCC; Fe_2O_3; Fe_3O_4; $FeCr_2O_4$; Cr_2O_3; $Cr_{1.3}Fe_{0.7}O_3$;
8000	BCC; Fe_2O_3; Fe_3O_4; $FeCr_2O_4$	BCC; Fe_2O_3; Fe_3O_4; Cr_2O_3; $FeCr_{1.5}Al_{0.5}O_4$	FCC; Fe_2O_3; Fe_3O_4; $FeCr_2O_4$; Cr_2O_3

3.2.2. *Ferritic alloy APMT*

Fig. 3 shows SEM-BSE images of ion milled cross-sections illustrating FeCrAl alloy APMT exposed for 168 h (Fig. 3a), 1000 h (Fig. 3b) and 8000 h (Fig. 3c). The shortest exposure duration (168 h) resulted in an approximately 25 µm thick oxide scale. The scale consists of an outward- and inward-growing layer illustrated by the dashed lines. The outward-growing layer is characterized by cracks and pores with large K_2CrO_4 particles embedded in it. SEM-EDS and SEM/EBSD analysis showed that the outward-growing scale was Fe-oxide consisting of hematite in region I and magnetite in region II. The inward-growing scale (region III) displays a variation in thickness ranging between 10 and 18 µm and has a spinel structure with a composition of 60 at% Fe, 15 at% Cr, 20 at% Al and minor elements (SEM/EDX and SEM/EBSD). Traces of Cl (less than

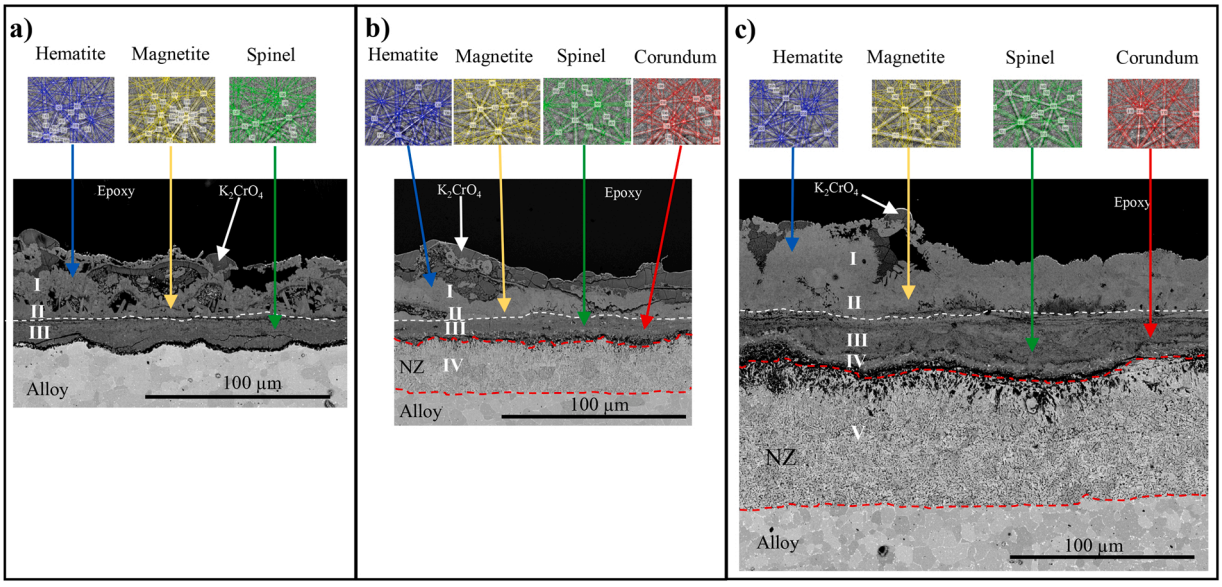

Fig. 3. SEM-BSE cross-section images of APMT after exposure for a) 168 h, b) 1000 h and c) 8000 h in 5% O_2 + 20% H_2O + N_2 (Bal) + KCl(s)/KCl(g) at 600 °C.

1-at%) were detected in the inward-growing oxide, but not in the outward-growing layer. K was detected in trace and elevated amounts (~5 at%) in the outer and inner scales respectively.

Exposure for 1000 h produced a 31 μm thick oxide scale with similar microstructural features as the scale formed after 168 h. In the surface region, larger K_2CrO_4 particles are observed (Fig. 3b). The outward-growing Fe-oxide is dense and consists of hematite in region I and magnetite in region II. The inward-growing scale (region III) was composed of 20 at% Fe, 55 at% Cr, 20 at% Al plus minor elements and was identified as spinel and corundum in different regions (see Fig. 3b) followed by a 12 μm deep depletion zone. Below the scale (region IV), a 28 μm thick nitridation zone (NZ) was formed. Traces of Cl (less than 1-at%) were detected in the inward-growing oxide, but not in the outward-growing layer. The presence of K was detected only in the outward-growing scale.

After 8000 h of exposure, the oxide scale is approximately 59 μm thick (Fig. 3c). The thickness ratio of the outward-growing scale and the inward-growing scale is about 50:50. Both hematite in region I and magnetite in region II are dense with very small pores. The inward-growing scale was composed of 20 at% Fe, 60 at% Cr, 20 at% Al and identified as spinel mixed with corundum. Closer to the metal-scale interface, a 6 μm thick layer with slightly lower Al content (25 at% Fe, 60 at% Cr, 15 at% Al) was identified (region IV). This was followed by 20 μm Cr-depletion zone. Below the scale, a 74 μm thick nitridation zone (NZ) was observed. Traces of Cl (less than 1-at%) were detected in the inward-growing oxide, but not in the outward-growing layer. The presence of K was detected only in the outward-growing scale.

3.2.3. *Austenitic stainless steel - Alloy 27Cr33Ni3Mo*

Fig. 4 shows SEM-BSE cross-sections of Alloy 27Cr33Ni3Mo after exposure durations 168 h (Fig. 4a), 1000 h (Fig. 4b) and 8000 h (Fig. 4c). The 27Cr33Ni3Mo alloy forms oxide scales with the same microstructural features as the other investigated alloys but in addition with a fine grain region (FGR) that is depleted in Cr and enriched in Ni.

After 168 h of exposure, Alloy 27Cr33Ni3Mo has formed a scale that is about 9 μm thick and dense in the upper and lower regions and contains pores in the middle regions (Fig. 4a). The SEM/EDS and SEM/EBSD investigation showed that the outward-growing oxide layer (region I) is composed of 40 at% Fe, 30 at% Cr, 30 at% Ni and was identified to have a spinel crystal structure. The inward-growing oxide scale (region II) is essentially the same kind of oxide consisting of spinel crystal structure with more Cr and less Fe (25 at% Fe, 50 at% Cr, 25 at% Ni). Trace amounts of Cl and K (less than 1 at%) were detected both in outward- and inward-growing oxides. Below the scale, the alloy forms a 4 μm deep Ni-rich fine grain region (region III) with average grains size of about 3 μm (the initial average alloy grain size was about 49 μm before starting the exposure). The fine grain region contains scattered voids.

After 1000 h exposure, the scale formed by Alloy 27Cr33Ni3Mo is in the same range as after 168 h, measuring 10 μm in thickness (Fig. 4b) while the K_2CrO_4 particles formed on the surface have become larger. The outward-growing oxide (region I) consists of spinel crystal structure with composition of 70 at% Fe, 30 at% Cr. The inward-growing has become enriched in Cr (20 at% Fe, 80 at% Cr) and consists of corundum crystal structure with a thickness of ~1.4 μm. Unoxidized metal regions are observed embedded in the lower regions of the inward-growing oxide. The voids formed below the scale have increased in number compared to the 168-hour exposure. The Ni-rich fine grain region (region III) has become deeper (13 μm deep) with average grain size of 3 μm.

After 8000 h of exposure, the scale has grown to 13 μm. The outward-growing scale is dense and consists of two distinguishable regions based on the contrast difference in the SEM/BSE image, i.e., light region I and dark region II. Region I is Fe-rich spinel with an average composition of 85 at% Fe, 15 at% Cr. The inward-growing scale (region II) is ~ 5.3 μm thick and consists of mixture of Cr-rich oxide islands with unoxidized Ni-rich metal regions. The Cr-rich oxide islands were identified as corundum and had a composition of 10 at% Fe, 90 at% Cr with average oxide grain size of 0.2 μm. The Ni-rich fine grain region (region III) beneath the scale has increased in thickness (~ 19 μm) and contains more voids along the grain boundaries. Traces of Cl (<1 at%) was detected in the inward-growing scale. K was detected in the outer scale

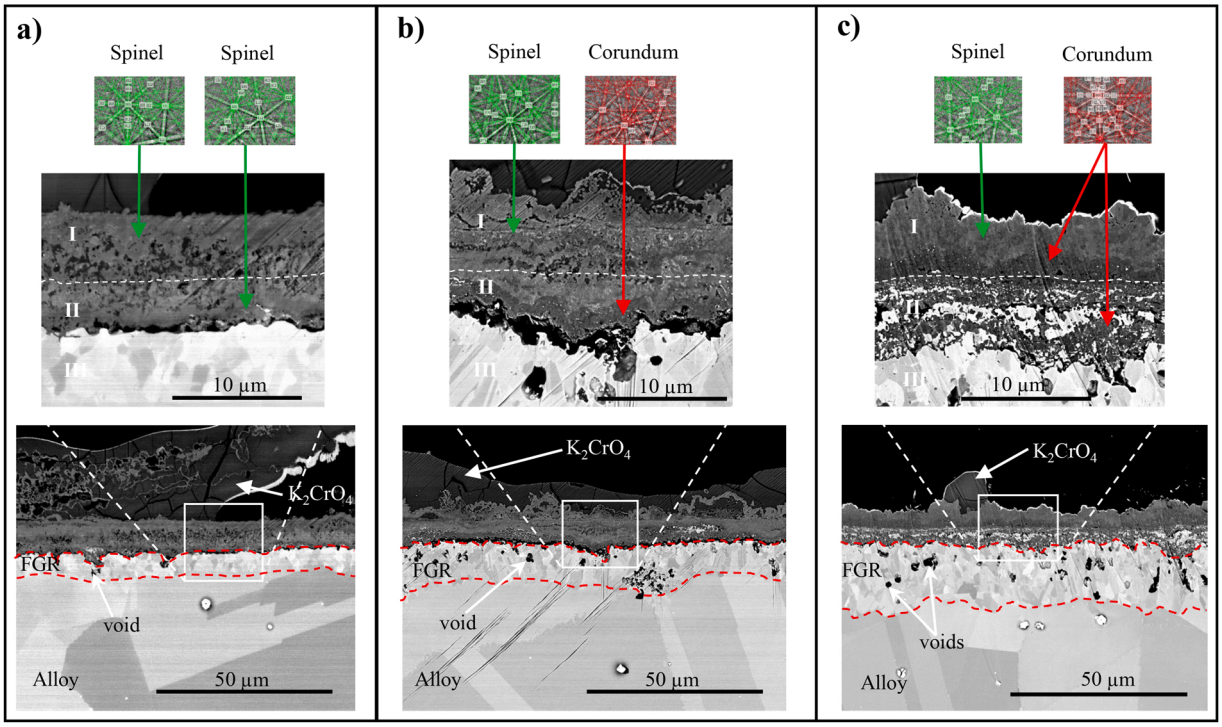

Fig. 4. SEM-BSE cross-section images of Alloy 27Cr33Ni3Mo after exposure for a) 168 h, b) 1000 h and c) 8000 h in 5% O_2 + 20% H_2O + N_2 (Bal) + KCl(s)/KCl(g) at 600 °C.

Table 3
Summary of results from microstructural investigation of SVM12, APMT and Alloy 27Cr33NiMo after exposure in 5 % O_2 + 20 % H_2O + N_2 (Bal) +KCl(s)/KCl (g) for 168 h, 1000 h and 8000 h.

Features	168 h	1000 h	8000 h
SVM12			
Scale thickness	91 μm	120 μm	206 μm
Potassium chromate	Apparent	Apparent	apparent
Average chemical composition	**Region I**: 100 at% Fe **Region II**: 95 at% Fe, 5 at% Cr **Region III**: 75 at% Fe, 25 at% Cr **Region IV**: 60 at% Fe, 40 at% Cr	**Region I**: 100 at% Fe **Region II**: 100 at% Fe **Region III**: 70 at% Fe, 30 at% Cr **Region IV**: 55 at% Fe, 45 at% Cr	**Region I**: 100 at % Fe **Region II**: 100 at % Fe **Region III**: 65 at % Fe, 35 at% Cr **Region IV**: 60 at % Fe, 40 at% Cr **Region V**: 35 at % Fe, 65 at% Cr
Crystalline phases	Hematite, magnetite, spinel	Hematite, magnetite, spinel	Hematite, magnetite, spinel
Cr-depletion below scale			14 μm deep
Presence of Cl	Yes (<1 at%) at the surface and inward-growing scale	Yes (<1 at%) at the surface and inward-growing scale	No
Presence of K	Yes (~1 at%) in outward-growing scale	Yes (~1 at%) in outward-growing scale	Yes (~1 at%) in outward-growing scale
Oxide grain size	1.5 μm	2.4 μm	14.1 μm
APMT			
Scale thickness	25 μm	31 μm	59 μm
Potassium chromate	Apparent	apparent	apparent
Average chemical composition	**Region I**: 90 at% Fe, 10 at% Cr **Region II**: 85 at% Fe, 15 at% Cr **Region III**: 60 at% Fe, 15 at% Cr, 20 at % Al, minor elements	**Region I**: 100 at% Fe **Region II**: 100 at% Fe **Region III**: 20 at% Fe, 55 at% Cr, 20 at % Al, minor elements **Region IV**: AlN	**Region I**: 100 at % Fe **Region II**: 100 at % Fe **Region III**: 20 at % Fe, 60 at% Cr, 20 at% Al **Region IV**: 25 at % Fe, 60 at% Cr, 15 at% Al **Region V**: AlN
Crystalline phases	Hematite, magnetite, spinel	Hematite, magnetite, spinel, Corundum	Hematite, magnetite, spinel, corundum
Cr-depletion below scale	Negligible	Yes (12 μm)	Yes (20 μm)
Presence of Cl	Yes, < 1 at% in inward-growing scale	Yes, (<1 at%) in inward-growing scale	Yes, < 1 at% in inward-growing scale
Presence of K	Outer scale: Yes (<1 at%) Inner scale: Yes (~5 at%)	Outer scale: Yes (<1 at%) Inner scale: No	Outer scale: Yes (<1 at%) Inner scale: No
Nitridation zone	No	Yes (28 μm)	Yes (74 μm)
Alloy 27Cr33Ni3Mo			
Scale thickness	9 μm	10 μm	13 μm
Potassium chromate	Apparent	Apparent	Apparent
Average chemical composition	**Region I**: 40 at% Fe, 30 at% Cr, 30 at % Ni **Region II**: 25 at% Fe, 50 at% Cr, 25 at % Ni	**Region I**: 70 at% Fe, 30 at% Cr **Region II**: 20 at% Fe, 80 at% Cr	**Region I**: 85 at% Fe, 15 at% Cr **Region II**: 10 at % Fe, 90 at% Cr **Region III**: 40 at % Fe, 15 at% Cr, 45 at% Ni
Crystalline phases	spinel	Spinel, corundum	Spinel, corundum
Cr-depletion below scale	Yes, about 4 μm deep	Yes, about 13 μm deep)	Yes (about 19 μm deep)
Grain refinement region	Yes, about 4 μm deep	Yes, about 13 μm deep	Yes (about 19 μm deep)
Presence of Cl	Yes, (<1 at%) in outward- and inward growing scales	Yes, < 1 at% in inward-growing scale	Yes, < 1 at% in inward-growing scale
Presence of K	Outer scale: Yes (~3 at%) Inner scale: Yes (~3 at%)	Outer scale: Yes (<1 at%) Inner scale: No	Outer scale: Yes (<1 at%) Inner scale: No

in less than 1 at%.

To summarize the findings of this study and highlight specific features of microstructural evolution of the scales formed by the investigated alloys, a summary of results is presented in Table 3.

3.3. Computational modelling

3.3.1. Thermodynamic calculations

In order to evaluate the behavior of the alloys, thermodynamic equilibrium calculations were performed to predict stable phases in what is interpreted as the inward-growing scale (low pO_2 range). It should be noted that in harsh environments where large amount of KCl is present, the interesting part from a calculation perspective is the corrosion front, i.e., at low pO_2 since the predicted primary protection (Cr_2O_3 or Al_2O_3) is rapidly broken down and the main part of the oxidation growth occurs after breakaway oxidation. Thermodynamic calculations predicting stable phases may therefore provide information about the low pO_2 range and the possibility to form internal oxidation/a slow growing Cr/Al-rich layer, i.e., the healing layer.

The stable phases have been plotted with variation of pO_2 to be able to predict the sequence of oxide phases for alloys SVM12, APMT and Alloy 27Cr33Ni3Mo and presented in Figs. 5, 6 and 7 respectively. The key phases have been marked to make it possible to systematically compare these alloys e.g., the inner part of the expected corrosion products for the different compositions for the three alloys with the observed microstructure.

Fig. 5, shows calculated equilibrium phase fractions against pO_2 for the oxide scale formed by SVM12. In the low oxygen partial pressure range, SVM12 forms various stable phases. In between $10^{-25} < pO_2 < 10^{-14}$, two spinel phases are predicted to form, spinel1 and spinel2 marked in red and blue colors respectively with spinel1 being the phase with higher amount (~ 90 %).

In $pO_2 < 10^{-25}$ regions (interpreted as the internal oxidation zone based on a combination of calculations and results from the microstructure investigation), a mixture of unreacted metal, spinel2 and a minor fraction of corundum type of oxide are predicted as the stable phases. The corundum phase forms close to the metal-scale interface with a fraction of ~ 22 %.

Fig. 6 shows calculated fractions of stable oxide phases against pO_2 for APMT. In the upper regions of the inward growing scale (interpreted to have $10^{-30} < pO_2 < 10^{-15}$), this alloy is predicted to form two spinel phases (spinel1 and spinel2) where spinel 1 is the major phase. Within the regions of $pO_2 < 10^{-25}$, unoxidized metal is predicted to be in equilibrium with the oxide phases. In lower oxygen partial pressure regions, i.e., $pO_2 < 10^{-30}$, the scale is composed of corundum type of oxide that is in equilibrium with unoxidized metal. The fraction of corundum-type oxide is ~ 44 %. For $pO_2 < 10^{-50}$, only the BCC is stable and is interpreted as the metal-scale interface.

The thermodynamic calculations predict that Alloy 27Cr33Ni3Mo forms multiphases in the inward-growing scale with oxygen partial pressure below 10^{-19}, see Fig. 7. In the range of $10^{-29} < pO_2 < 10^{-19}$, spinel is the major phase with a fraction of a ~ 90 % and in equilibrium

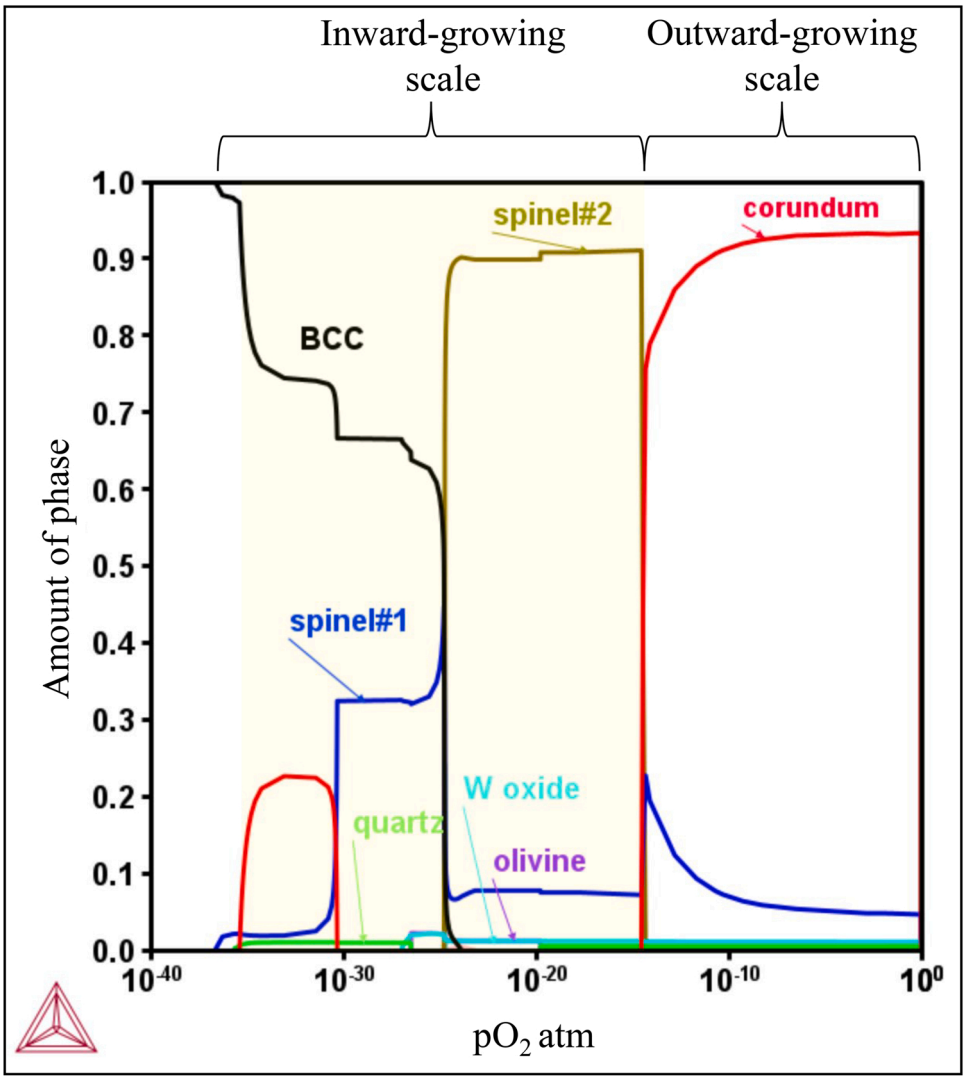

Fig. 5. Thermodynamic equilibrium calculations showing the amount of predicted stable phases plotted against pO_2 for SVM12.

with unoxidized metal. In the inner regions (pO_2 $<10^{-29}$), corundum type of oxide is predicted to form with a fraction of 46 %.

3.3.2. *Kinetic simulations*

The kinetic simulations show the potential of predicting both protective and non-protective oxide scale growth kinetics. Dictra simulations following the method suggested in [31] were used to predict the oxidation kinetics after long-term exposures, i.e., the reformation of a Cr_2O_3 type of scale in the bottom of the inward growing scale observed on Alloy 27Cr33Ni3Mo. The starting time for the formation of the corundum phase is somewhere between 168 h (not observed in the carful microstructural investigation) and 1000 h where it is observed to be 1.4 μm. To be able to easier evaluate the growth kinetics between 1000 h and 8000 h, the simulated curve was shifted in time so that the thickness after 1000 h matches the experimental observation. The starting time for the shifted simulated curve may be used as an indication for the formation of corundum phase but is not considered to be correct. The simulated curve adds value by contributing to the kinetics of a simulated external scale between 1000 h and 8000 h for comparison with the experimental observation. Fig. 8 shows the results of the corundum phase growth kinetics obtained through simulation implementing the grain size observed in the microstructure investigation and starting the simulation of the protective corundum structure after 1000 h up to 8000 h of exposure. The simulated growth rate known to predict an external Cr_2O_3 scale very well at this temperature [31] indicate slower kinetics than the scale formed on Alloy 27Cr33Ni3Mo.

4. Discussion

Three different alloys have been selected for this study in order to study the corrosion properties in harsh environments for long durations. The alloys represent three different material classes that may be used in these environments and applications, i.e., SVM12 (representing martensitic stainless steel), APMT (representing FeCrAl alloys) and Alloy 27Cr33Ni3Mo (representing austenitic stainless steel). It may be noted that these alloys/or alloys of similar composition form a slow growing chromia/alumina scale at 600 °C in the absence of KCl/H_2O [32–34]. The focus of this investigation has been to study the oxide features beyond breakaway in presence of KCl/H_2O (i.e., the secondary corrosion regime) in order to understand the corrosion mechanisms for long durations and protectiveness of these scales after breakaway oxidation. This is reflected in the investigation of oxide kinetics following breakaway oxidation as well as the oxide microstructure evolution after the breakaway oxidation.

4.1. *Oxidation kinetics*

The experimental setup mimicking key components in the aggressive

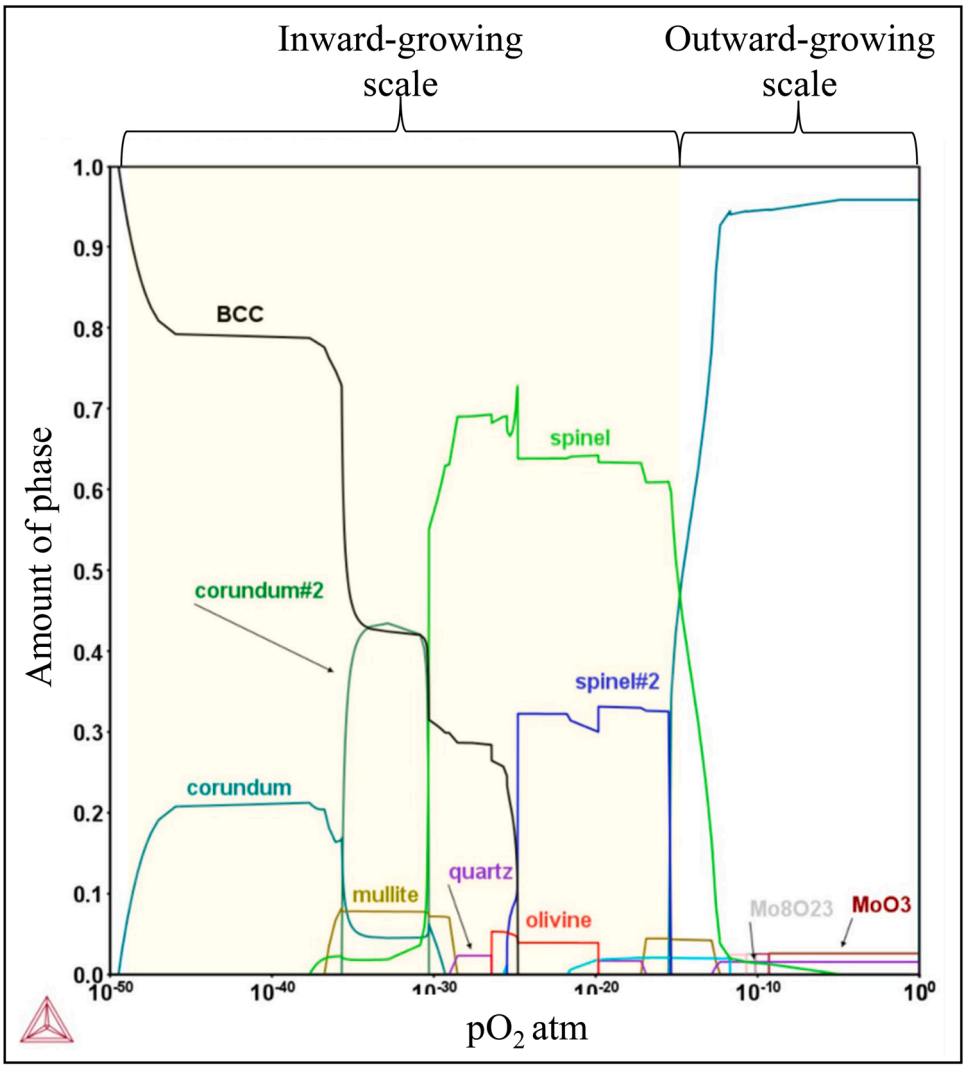

Fig. 6. Thermodynamic equilibrium calculations showing the amount of predicted stable phases plotted against pO_2 for APMT.

environment found in the biomass-and waste-fired boilers was used to trigger fast breakaway oxidation of the three different alloys. The combustion of biomass and waste creates corrosive species such as KCl and water vapor that have been reported to accelerate corrosion of the metallic components and transform the protective scales into fast-growing and less protective scales, see e.g., [6,7,10,35,36]. In recent studies where oxide scales formed prior and just after breakaway oxidation have been investigated, the concepts of primary and secondary corrosion regimes were introduced to elucidate the different corrosion modes that a material can undergo during the oxidation/corrosion process [17,19,37] where the primary and secondary refer to the corrosion regimes before and after breakaway oxidation respectively. The experimental setup in addition secures the presence of the corrosive components during all of the long exposures, i.e., for all duration in the secondary regime after breakaway oxidation [25]. This is supported by the presence of KCl on the surface of all samples after all durations.

The oxidation kinetics to be discussed in this section are based on measured oxide thicknesses and not mass gains as these may cause challenges due to evaporation/spallation during long time exposures (Fig. 1). The Broad Ion Beam milling offers a very good experimental setup to gently create a very wide cross-section for thickness measurements providing accurate interpretations of the thickness variations as well as the microstructural evolution. The results show that all the alloys have experienced breakaway oxidation after the shortest exposure time, i.e., already after 168 h as expected in the presence of KCl/H_2O. The kinetics/evolution of oxide microstructure described below after 168 h corresponds to the secondary regime.

The marginal chromia former SVM12 (12 wt% Cr) exhibits the fastest oxide growth rate indicating a fast initial breakdown of the primary oxide (Cr rich scale) in combination with fast oxide growth following breakaway, i.e., formation of a poor secondary protection. The fast oxidation kinetics observed in current study are in line with kinetics of pure iron oxidation without the formation of FeO [38]. This may be attributed to the limited supply of alloying elements such as Cr to the corrosion front that otherwise may contribute to the re-formation of a protective scale and mitigate further rapid corrosion. Comparable findings have been reported for several alloys with similar composition exposed in aggressive environment [17,39,40]. Fast oxidation kinetics have in addition been explained by the mechanism ‘‘active oxidation’’ which postulates that chlorine acts as catalyst and accelerates the degradation of the metal as the volatile metal chlorides diffuse outwards through the porous scale, see e.g., [41–43]. However, the oxide microstructures formed by all alloys in this study are dense, which indicates that the scale growth is controlled by the outward/inward diffusion of cations/anions through the scale, see microstructures in Figs. 2, 3 and 4. Furthermore, the oxidation kinetics ($\alpha > 2$) for SVM12 indicate sub-parabolic growth behavior. The sub-parabolic oxidation behavior may be explained by oxide grain growth which slows down the oxidation process and/or the formation of a protective scale formed at the metal/oxide interface after some time.

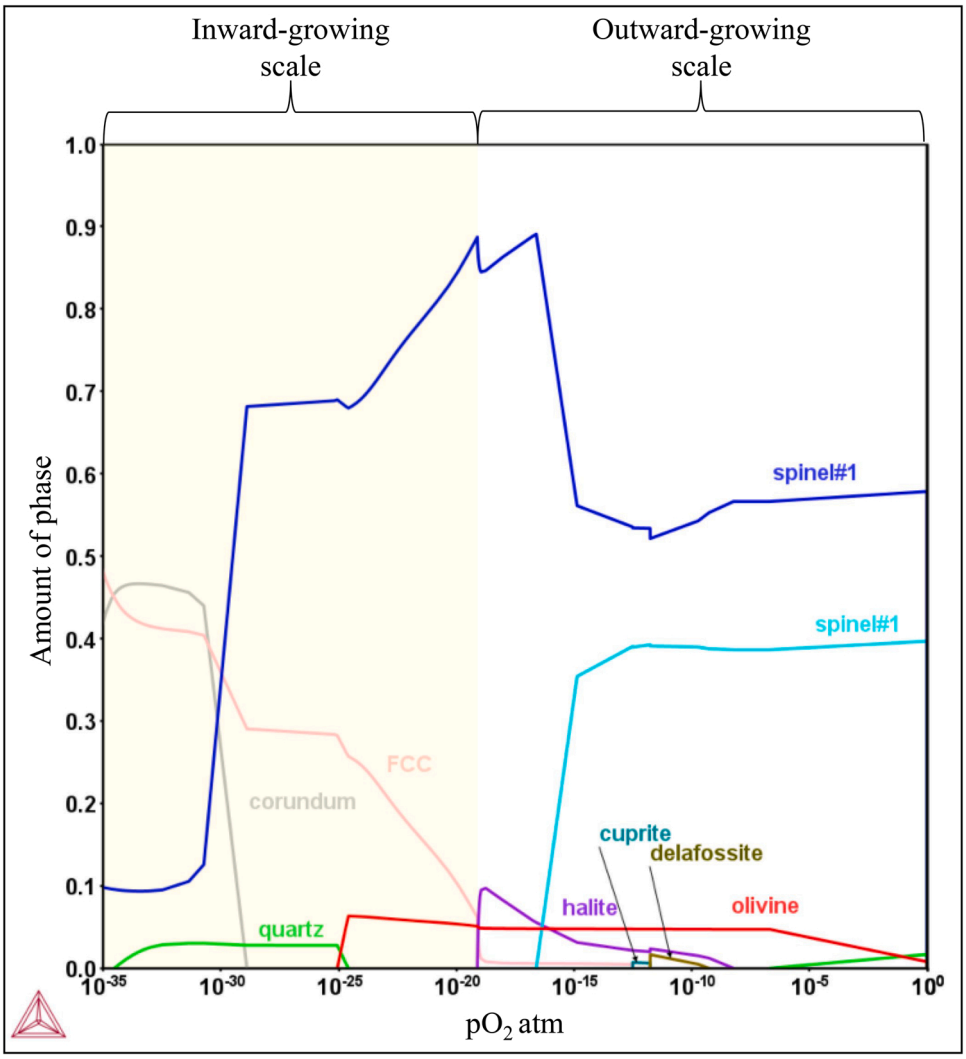

Fig. 7. Thermodynamic equilibrium calculations showing the amount of predicted stable phases plotted against pO_2 for Alloy 27Cr33Ni3Mo.

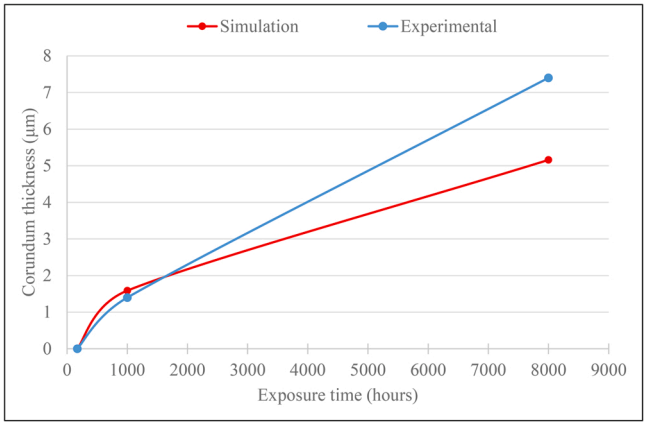

Fig. 8. Growth kinetics of the Cr-rich corundum oxide in the inward-growing scale of Alloy 27Cr33Ni3Mo.

For the high Cr-content alloys (APMT and Alloy 27Cr33Ni3Mo), slower oxidation kinetics following breakaway oxidation is observed. The α values for both alloys are larger than for SVM12, which indicates that these high-alloyed steels transition into sub-parabolic behavior early and experience slow corrosion rates. However, this deviation may not be explained by iron oxide grain growth. The variation in oxidation kinetics between the marginal chromia former SVM12 and the high alloyed steels may instead be linked to the oxide microstructure formed after breakaway oxidation.

4.2. *Microstructural evolution of poor secondary protection*

Microstructural investigation of the oxides formed by SVM12 (12 % Cr), revealed that this alloy forms a dense and thick oxide scale (91 µm) already after 168 h of exposure. The scale has similar microstructure after all exposures but grows to more than double the thickness after 8000 h, see Fig. 2. The formation of thick scales is associated with the scale formed after breakaway oxidation where the alloy transitions into the secondary corrosion regime, i.e., forms fast-growing Fe-rich oxide in the outer scale and inward-growing spinel as a result of different diffusivities of the alloying elements in the spinel [44]. The thick oxide scales formed by SVM12 in this case indicate that this alloy exhibits a poor secondary protection after breakaway. Indeed, after the shortest exposure time, this alloy has formed a duo-layered scale that consists of Fe-rich oxides (hematite and magnetite) in the outward-growing scale as Fe diffuses orders of magnitude faster than e.g. Cr, and inward-growing spinel which is enriched in all other alloying elements, similar to the oxide microstructures reported for many steels after breakaway, see e.g., [17,23,39,45–47]. The crystalline oxide phases identified from experimental investigation using XRD and EBSD agree with the results of

thermodynamic equilibrium calculations which predicts spinel as the major phase in the inward-growing scale. Although the composition of each phase was not calculated, the SEM/EDS elemental analysis indicates that it is a FeCr-spinel and that the Cr concentration increases with time, see summary results in Table 3.

The microstructural investigation revealed that growth rate is dominated by iron and oxygen diffusion which results in sub-parabolic oxidation kinetics after very long exposures. This may be explained by the results of the oxide grain measurements in the outward growing iron oxide which showed grain growth from 1.5 μm to 2.4–14.1 μm after 168 h, 1000 h and 8000 h as well as indications of a more Cr rich scale at the metal/oxide interface after 8000 h. The fast kinetics and the sub-parabolicity indicate a diffusion-controlled behavior that may be associated with a high outward flux of Fe via grain boundaries of the formed Fe-rich spinel (magnetite). Similar observations have been reported for the oxidation of pure iron at 600 °C [48] and other alloys [49–51]. It is suggested that oxide grain coarsening leads to reduced number of diffusion pathways for ions which in turn slows down the scale growth. The regions closer to the scale/metal interface becomes enriched in Cr with exposure time reaching up to 65 at% after 8000 h (see region V in Fig. 2c) followed by a 14 μm deep Cr-depletion zone. The Cr-enriched regions may form in the internal oxidation zone ($pO_2 < 10^{-25}$) where thermodynamic calculations predict the formation of a spinel type of oxide while internal oxidation with a corundum phase is predicted at a lower pO_2 ($pO_2 < 10^{-30}$), see Fig. 5. However, SEM/EBSD and XRD analyses showed absence of corundum phase in these regions. This alloy has a limited supply of Cr to the corrosion front which prevents it from forming a more protective oxide, i.e., a corundum-type oxide. The formation of protective scale is associated with high content of Cr/Al elements in the alloy which elevates (Cr,Al)/Fe ratio in the oxide [39]. It may be noted that even though the alloy exhibits a deep Cr depletion in the regions below the scale/metal interface, the inner scale is only composed of at the most 65 at% Cr closer to the metal/scale interface. Very small amounts of K, Cl could be observed in the scale and no indication of active oxidation in the microstructure. On the contrary, the microstructural investigation shows that the growth rate is diffusion controlled while the small amounts of K and Cl detected in the investigation could increase the diffusivity of iron and oxygen.

4.3. Microstructural evolution of good secondary protection

Within the secondary corrosion regime, an alloy is considered to form a good secondary protection if the oxide scale formed after breakaway oxidation is slow-growing and can reduce the rate of oxidation of the alloy [17]. Microstructural investigation of the oxide scales formed by the high alloyed APMT and the austenitic Alloy 27Cr33Ni3Mo after all exposure times revealed that the scales are duo-layered, i.e., consisting of outward- and inward-growing layers (see Figs. 3 and 4) which shows that the alloys have experienced breakaway oxidation and transitioned into the secondary corrosion regime already after 168 h-exposure. However, in contrast to the marginal chromia former SVM12 discussed in the previous section, these alloys exhibit much slower oxidation rates and form healing layer of Cr/Al-rich inward-growing scales which provide a good secondary protection in this environment.

In the case of APMT, the SEM/EDS, SEM/EBSD and XRD analysis show that during the first 168 h of exposure, the alloy forms a scale that consists of Fe-rich oxides (hematite and magnetite) in the outward-growing scale and a spinel in the inward-growing scale (see Fig. 3). The SEM/EDS results show that as oxidation progresses, the inner scale becomes enriched in Cr and that the alloy is depleted in Cr beneath the scales (12 μm and 20 μm deep after exposure for 1000 and 8000 h respectively). The increased Cr content at the metal/oxide interface is in this case not only caused by the diffusion of iron but also a consequence of supply from the bulk alloy. It may be noted that the concentrations of Cr and Al cations in the inner scales of APMT after 1000 h and 8000 h of exposure exceed 67.7 at% cations, i.e., exceeding the maximum limit for the concentration of trivalent ions in a spinel structure. A higher concentration would only be possible in a corundum structure where the trivalent cations occupy the octahedral vacancy sites [52,53]. Indeed, the crystalline phase identification using SEM/EBSD and XRD revealed the presence of corundum-type oxide in the inner scales. These changes in oxide microstructure may explain the improved corrosion resistance displayed by this alloy within the secondary corrosion regime. The transition of the inward growing spinel from an iron source, as for SVM12, may be associated with the higher level of Cr in the spinel as well as the activity in the bulk. The results are in line with findings of other studies where it has been shown that the alloying elements Cr and Al have beneficial effect in mitigating the corrosion process of alloys [17,19,25,54,55]. The experimental data in addition agree with the thermodynamic calculations which predicts the formation of spinel phase in the upper regions of the inward-growing scale and corundum phase in lower pO_2 ($pO_2 < 10^{-30}$). The co-existence of spinel with the corundum phase has been suggested to be the foundation for a good secondary protection [56] and will together with continuous supply of Cr to the corrosion front speed up the transition to higher corundum phase fraction in the inner scale.

Another interesting characteristic feature of oxidation of APMT is the formation of the nitridation zones (NZ) beneath the scales. SEM/EDS results showed that this alloy forms NZ after 1000 h (28 μm) and 8000 h (74 μm), but not after 168 h (see Fig. 3). Alloy nitridation is a phenomenon that has been widely reported in literature, see e.g., [23,57–59]. Nitridation occurs due to defects in the scale which enable N to diffuse into the alloy [59]. In the current study, the formation of NZ by APMT indicates that the scales formed are permeable to N. One consequence of this process is that aluminum gets trapped as aluminum nitrides (AlN) which could have negative effect on the corrosion behavior of the alloy and the mechanical properties of the alloy. The absence of NZ after the shortest exposure time (168 h) in this study is not surprising as similar observations have been made for the same material after exposure in similar environment [59,60]. A possible explanation provided by the authors of [60] is that the processes of aluminum nitride formation could be retarded by the slow processes of N_2 dissociation, dissolution, and nitride nucleation. Regarding the mechanical properties, an increase in internal precipitates of AlN may result into alloy embrittlement [61] and impaired ductility [62] which consequently affects material performance. Although the effect of nitridation on corrosion behavior of the alloy was not further investigated in this study, the authors note that there is need for more research to fully understand the mechanism and the effect of this process on corrosion of high temperature alloys.

In the case of Alloy 27Cr33Ni3Mo, the results show that this alloy has the best secondary corrosion protection among the investigated alloys. The growth kinetics is several orders of magnitude slower than the SVM12 alloy. The duo-layered scale that initially consists of Fe/Ni-rich spinel in the outer scale and a Cr-rich spinel in the inner scale (after 168 h) exhibits Cr-enrichment in the inner scale after longer exposures and transforms into a very Cr-rich corundum-type oxide between 168 and 1000 h. The good secondary protection exhibited by this alloy is attributed to the high content of Cr in the alloy in combination with a microstructure change in the alloy resulting in fast diffusion pathways to the oxide scale which makes it possible for the alloy to replenish Cr in the oxide and form the protective scale.

According to the equilibrium calculations, the inward-growing scale is predicted to contain regions of unreacted metal together with spinel and corundum-type oxide at the lowest oxygen partial pressure regions. These modelling results agree well with the experimental results of this study. After 1000 h, corundum phase is only detected in the lower regions with a measured thickness of ~1.4 μm, which increases to ~ 5.3 μm after 8000 h. In order to evaluate the oxidation kinetics of this alloy, the corundum scale observed in the metal/oxide interface was in addition simulated using DICTRA. As Fig. 8 shows, the experimental

oxidation kinetics are somewhat faster than the simulated kinetics between 1000 h and 8000 h. A deviation from the growth kinetics of the outer scale is expected as the scale growing in the bottom of a thicker scale is governed by inward diffusion of oxygen and Cr diffusion/supply as well as a possible phase transformation from a Cr-rich spinel into the corundum phase. This is in line with the observations of a previous study where it was observed that the inner scale of the Fe20CrAlSi alloy became enriched in corundum phase after exposure for 2000 h indicating a similar phase transformation [56]. The faster kinetics of the corundum formation and the slow kinetics of the overall scale indicate that the thickness of the external scale (spinel oxide) reduces as the oxidation progresses which shows very protective properties of the healing layer. The formation of a Cr-rich corundum phase may explain the very protective properties of the scale formed on Alloy 27Cr33Ni3Mo within the secondary corrosion regime.

Another interesting microstructural feature of Alloy 27Cr33Ni3Mo is the formation of fine grain region (FGR) beneath the scale. The FGR in addition grows with exposure time, i.e., from 4 μm to 19 μm after 168 and 8000 h respectively, see Fig. 4a and c. Although the mechanism behind the formation of the FGR region was not established in this study, it may be noted that these fine grains have a large influence on the corrosion behavior providing fast diffusion paths for Cr from the bulk to the protective Cr-rich scale. It may in this context be noted that the fine grain regions were Cr depleted (and Ni-enriched). The phenomenon of alloy grain refinement has been reported in literature and has been suggested to enhance grain boundary diffusion due to the increased diffusion pathways for ions [63–66]. On the other hand, the fast flux of Cr from the alloy was observed to be associated with void formation in the Cr-depleted FGR, see micrographs in Fig. 4. The concentration and size of these voids increase with exposure time. Void formation is attributed to the different diffusion coefficients of Cr and Ni in the alloy matrix where the former diffuses faster to the metal/scale interface leaving behind agglomerates of vacancies (voids) in the Ni-enriched regions awing to the Kirkendall effect. Void formation in nickel containing alloys has been reported in several studies from both experimental work [67] and modelling [68]. The void may have a negative effect reducing the ability of the alloy to form adhesive scale.

5. Conclusion

In this study, the long-term corrosion behavior of SVM12, APMT and Alloy 27Cr33Ni3Mo was investigated through exposures in a KCl-rich environment at 600 °C for 168, 1000 and 8000 h with advanced electron microscopy and thermodynamic modelling. The concepts of poor and good secondary protection were adopted to refer to non-protective and protective oxide scales formed after breakaway oxidation. Oxide thickness measurements showed that SVM12 experienced rapid oxide growth and formed thick scales which indicated poor secondary protection that is diffusion controlled. APMT and Alloy 27Cr33Ni3Mo exhibited slow oxidation kinetics and formed thin scales which indicated good secondary protection. The variation in oxidation kinetics and corrosion resistance among the alloys was mainly due to the different oxide microstructures formed after breakaway oxidation.

Microstructural investigation showed that all the alloys experienced breakaway oxidation after all exposure durations and formed duo-layered scales consisting of outward- and inward-growing scales. SVM12 formed fast-growing Fe-rich oxides in outer scales and spinel in the inner scales in all exposures. The poor secondary protection exhibited by this alloy was attributed to limited chromium content in the alloy. APMT and Alloy 27Cr33Ni3Mo formed Fe-rich oxides in outer scales and spinel in inner scale after 168 h. However, as the oxidation progressed, the inward-growing scales of both alloys became enriched in chromium/aluminum and the spinel transforms into corundum-type oxide. The experimental data agreed well with the results of thermodynamic calculations which predict stable oxide phases at equilibrium. The simulated oxidation kinetics for Alloy 27Cr33Ni3Mo was slower than the experimental result which indicated phase transformation within the inward-growing scale.

Funding

This study was supported by EC for financial support within the frame of the Horizon 2020 project “Lowering Costs by Improving Efficiencies in Biomass Fueled Boilers: New Materials and Coatings to Reduce Corrosion (BELENUS)”, Grant Agreement number: 815147.

CRediT authorship contribution statement

Vicent Ssenteza: Conceptualization, Methodology, Investigation, Data curation, Validation, Writing – original draft, Writing – review & editing. **Johan Eklund:** Conceptualization, Validation, Writing – review & editing. **Sedigheh Bigdeli:** Investigation, Data curation, Writing – review & editing. **Torbjörn Jonsson:** Conceptualization, Writing – review & editing, Supervision, Project administration.

Declaration of Competing Interest

The authors declare that they have no known competing financial interests or personal relationships that could have appeared to influence the work reported in this paper.

Data availability

Data will be made available on request.

Acknowledgements

This study was carried out at the High Temperature Corrosion Centre (HTC) at Chalmers University of Technology. The microscopy work was performed at Chalmers Materials Analysis Laboratory (CMAL).

References

[1] H.P. Nielsen, F.J. Frandsen, K. Dam-Johansen, L.L. Baxter, The implications of chlorine-associated corrosion on the operation of biomass-fired boilers, Prog. Energy Combust. Sci. 26 (2000) 283–298, https://doi.org/10.1016/S0360-1285(00)00003-4.

[2] K.O. Davidsson, L.-E. Åmand, B. Leckner, B. Kovacevik, M. Svane, M. Hagström, J. B.C. Pettersson, J. Pettersson, H. Asteman, J.-E. Svensson, L.-G. Johansson, Potassium, Chlorine, and Sulfur in Ash, Particles, Deposits, and Corrosion during Wood Combustion in a Circulating Fluidized-Bed Boiler, (2007). ⟨https://doi.org/10.1021/ef060306c⟩.

[3] J. Eklund, J. Phother, E. Sadeghi, S. Joshi, J. Liske, High-temperature corrosion of HVAF-sprayed Ni-based coatings for boiler applications, Oxid. Met. 91 (2019) 729–747, https://doi.org/10.1007/s11085-019-09906-0.

[4] Y. Alipour, P. Henderson, Corrosion of furnace wall materials in waste-wood fired power plant, Corros. Eng., Sci. Technol. 50 (2015) 355–363, https://doi.org/10.1179/1743278214Y.0000000228.

[5] J. Pettersson, Alkali induced high temperature corrosion of stainless steel-experience from laboratory and field, Chem. Chem. Eng. (2008) https://doi.org/ISBN:978-91-7385-214-2.

[6] J. Pettersson, C. Pettersson, H. Asteman, J.-E. Svensson, L.-G. Johansson, A pilot plant study of the effect of alkali salts on initial stages of the high temperature corrosion of alloy 304L, Mater. Sci. Forum 461–464 (2004) 965–972.

[7] J. Eklund, B. Paz, J. Maria Dolores Jönsson, J.-E. Liske, T.J. Svensson, Field exposure of FeCrAl model alloys in a waste-fired boiler at 600°C: The influence of Cr and Si on the corrosion behaviour, Mater. Corros. 70 (2019) 1476–1485.

[8] J. Eklund, M. Dolores Paz, B. Jönsson, Jesper Liske, J.-E. Svensson, T. Jonsson, Field Exposure of FeCrAl Model Alloys in A Waste-fired Boiler at 600°C: the influence of Cr and Si on the Corrosion Behaviour, (2019). ⟨https://doi.org/10.1002/maco.201810618⟩.

[9] T. Jonsson, S. Karlsson, H. Hooshyar, M. Sattari, J. Liske, J.-E. Svensson, L.-G. Johansson, Oxidation after breakdown of the chromium-rich scale on stainless steels at high temperature: internal oxidation, Oxid. Met. 85 (2016) 509–536, https://doi.org/10.1007/s11085-016-9610-7.

[10] J. Phother-Simon, T. Jonsson, J. Liske, Continuous KCl addition in high temperature exposures of 304 L – a way to mimic a boiler environment, Corros. Sci. 167 (2020), 108511, https://doi.org/10.1016/J.CORSCI.2020.108511.

[11] S.C. Okoro, S. Kiamehr, M. Montgomery, F.J. Frandsen, K. Pantleon, Effect of flue gas composition on deposit induced hightemperature corrosion under laboratory conditionsmimicking biomass firing. Part I: exposures in oxidizingand chlorinating

atmospheres, Mater. Corros. 68 (2017) 499–514, https://doi.org/10.1002/maco.201609173.
[12] T.M. Meißner, X. Montero, D. Fähsing, M.C. Galetz, Cr diffusion coatings on a ferritic-martensitic steel for corrosion protection in KCl-rich biomass co-firing environments, Corros. Sci. 164 (2020), 108343, https://doi.org/10.1016/J.CORSCI.2019.108343.
[13] D.L. Wu, K.V. Dahl, F.B. Grumsen, T.L. Christiansen, M. Montgomery, J. Hald, Breakdown mechanism of γ-Al2O3 on Ni2Al3 coatings exposed in a biomass fired power plant, Corros. Sci. 170 (2020), 108583, https://doi.org/10.1016/J.CORSCI.2020.108583.
[14] D. Fantozzi, V. Matikainen, M. Uusitalo, H. Koivuluoto, P. Vuoristo, Chlorine-induced high temperature corrosion of Inconel 625 sprayed coatings deposited with different thermal spray techniques, Surf. Coat. Technol. 318 (2017) 233–243, https://doi.org/10.1016/J.SURFCOAT.2016.12.086.
[15] E. Essuman, G.H. Meier, J. Zurek, M. Hänsel, L. Singheiser, W.J. Quadakkers, Enhanced internal oxidation as trigger for breakaway oxidation of Fe–Cr alloys in gases containing water vapor, Scr. Mater. 57 (2007) 845–848, https://doi.org/10.1016/J.SCRIPTAMAT.2007.06.058.
[16] X. Montero, A. Ishida, M. Rudolphi, H. Murakami, M.C. Galetz, Breakaway corrosion of austenitic steel induced by fireside corrosion, Corros. Sci. 173 (2020), 108765, https://doi.org/10.1016/j.corsci.2020.108765.
[17] A. Persdotter, J. Eklund, J. Liske, T. Jonsson, Beyond breakaway corrosion – influence of chromium, nickel and aluminum on corrosion of iron-based alloys at 600 °C, Corros. Sci. 177 (2020), 108961, https://doi.org/10.1016/j.corsci.2020.108961.
[18] R. Zhou, F. Wang, K. Xu, Y. Yuan, L. Chen, M. Lou, A.V. Khvan, K. Chang, Effect of molybdenum addition on oxidation behavior and secondary protection mechanism of FeCrAl coatings, Mater. Charact. 204 (2023), 113221, https://doi.org/10.1016/J.MATCHAR.2023.113221.
[19] J. Eklund, A. Persdotter, I. Hanif, S. Bigdeli, T. Jonsson, Secondary corrosion protection of FeCr(Al) model alloys at 600 °C – The influence of Cr and Al after breakaway corrosion, Corros. Sci. 189 (2021), 109584, https://doi.org/10.1016/J.CORSCI.2021.109584.
[20] A. Col, V. Parry, C. Pascal, Oxidation of a Fe–18Cr–8Ni austenitic stainless steel at 850 °C in O2: microstructure evolution during breakaway oxidation, Corros. Sci. 114 (2017) 17–27, https://doi.org/10.1016/j.corsci.2016.10.029.
[21] Y.C. Malede, J.P. Simon, T. Jonsson, M. Montgomery, K.V. Dahl, J. Hald, KCl-induced corrosion of Ni-based alloys containing 35–45 wt% Cr, Mater. Corros. 70 (2019) 1486–1506, https://doi.org/10.1002/maco.201810658.
[22] J.-H. Kim, D.-I. Kim, S. Suwas, E. Fleury, K.-W. Yi, J.-H. Kim, D.-I. Kim, E. Fleury, K.-W. Yi, S. Suwas, Grain-size effects on the high-temperature oxidation of modified 304 austenitic stainless steel, Oxid. Met. 79 (2013) 239–247, https://doi.org/10.1007/s11085-012-9347-x.
[23] J. Eklund, I. Hanif, S. Bigdeli, T. Jonsson, High temperature corrosion behavior of FeCrAlSi model alloys in the presence of water vapor and KCl at 600 °C – the influence of Cr content, Corros. Sci. 198 (2022), 110114, https://doi.org/10.1016/J.CORSCI.2022.110114.
[24] M. Subanović, J. Pirón, F. Zeller, M. Jarrar, A. Schneider, Super VM12 - a new 12% Cr Boiler Steel, in: J. Shingledecker, M. Takeyama (Eds.), in: Proceedings of the Joint EPRI – 123HiMAT International Conference on Advances in High Temperature Materials, ASM International, 2019, pp. 205–216, https://books.google.se/books?id=zbq9DwAAQBAJ&lpg=PA207&vq=SuperVM12&pg=PA205#v=snippet&q=Super VM12 &f=false.
[25] V. Ssenteza, J. Eklund, I. Hanif, J. Liske, T. Jonsson, High temperature corrosion resistance of FeCr(Ni, Al) alloys as bulk/overlay weld coatings in the presence of KCl at 600 °C, Corros. Sci. 213 (2023), 110896, https://doi.org/10.1016/J.CORSCI.2022.110896.
[26] ASTM international, Standard Test Methods for Determining Average Grain Size, PA 19428–2959, 2013. https://doi.org/Designation: E112–12.
[27] B. Sedigheh, R. Naraghi, A. Harihara Subramonia Iyer, T. Jonsson, Thermodynamic and Kinetic Assessment of Binary Cr-O: Case Study for Effect of Grain Size in the Oxide Growth Rate, n.d.
[28] J.-O. Andersson, T. Helander, L. Höglund, P. Shi, B. Sundman, Thermo-Calc & DICTRA, computational tools for materials science, Calphad 26 (2002) 273–312, https://doi.org/10.1016/S0364-5916(02)00037-8.
[29] C. Jiang, M. Feng, M. Chen, K. Chen, S. Geng, F. Wang, Corrosion behaviour of iron and nickel aluminide coatings under the synergistic effect of NaCl and water vapour, Corros. Sci. 187 (2021), 109484, https://doi.org/10.1016/j.corsci.2021.109484.
[30] K. Chandra, I. Dörfel, N. Wollschläger, A. Kranzmann, Microstructural investigation using advanced TEM techniques of inner oxide layers formed on T92 steel in oxyfuel environment, Corros. Sci. 148 (2019) 94–109, https://doi.org/10.1016/j.corsci.2018.12.008.
[31] S. Bigdeli, L. Kjellqvist, R. Naraghi, L. Höglund, H. Larsson, T. Jonsson, Strategies for high-temperature corrosion simulations of Fe-based alloys using the Calphad approach: part I, J. Phase Equilibria Diffus 42 (2021) 403–418, https://doi.org/10.1007/s11669-021-00893-x.
[32] T. Olszewski, Oxidation Mechanisms of Materials for Heat Exchanging Components in CO2/H2O-containing Gases Relevant to Oxy-fuel Environments, Forschungszentrum, Zentralbibliothek, 2012. ⟨https://books.google.se/books?id=rKA0_6HmjMwC⟩.
[33] K. Oh, K. Eom, Z. Liang, P.M. Singh, High temperature oxidation behavior of APM and APMT under dry air/steam condition, MRS Adv. 1 (2016) 2471–2476, https://doi.org/10.1557/adv.2016.514.
[34] C. Pettersson, T. Jonsson, C. Proff, M. Halvarsson, J.-E. Svensson, L.-G. Johansson, High temperature oxidation of the austenitic (35Fe27Cr31Ni) alloy Sanicro 28 in O2 + H2O environment, Oxid. Met. 74 (2010) 93–111, https://doi.org/10.1007/s11085-010-9199-1.
[35] J. Sui, J. Lehmusto, M. Bergelin, M. Hupa, The effects of KCl, NaCl and K2CO3 on the high-temperature oxidation onset of Sanicro 28 steel, Oxid. Met. 85 (2016) 565–598, https://doi.org/10.1007/s11085-016-9613-4.
[36] R. Jafari, E. Sadeghimeresht, T.S. Farahani, M. Huhtakangas, N. Markocsan, S. Joshi, KCl-induced high-temperature corrosion behavior of HVAF-sprayed Ni-based coatings in ambient air, J. Therm. Spray. Technol. 27 (2018) 500–511, https://doi.org/10.1007/s11666-017-0684-9.
[37] J. Phother-Simon, I. Hanif, J. Liske, T. Jonsson, The influence of a KCl-rich environment on the corrosion attack of 304 L: 3D FIB/SEM and TEM investigations, Corros. Sci. 183 (2021), 109315, https://doi.org/10.1016/J.CORSCI.2021.109315.
[38] B. Pujilaksono, T. Jonsson, M. Halvarsson, J.-E. Svensson, L.-G. Johansson, Oxidation of iron at 400–600 °C in dry and wet O2, Corros. Sci. 52 (2010) 1560–1569, https://doi.org/10.1016/J.CORSCI.2010.01.002.
[39] B. Pujilaksono, T. Jonsson, H. Heidari, M. Halvarsson, J.-E. Svensson, L.-G. Johansson, Oxidation of binary FeCr alloys (Fe–2.25Cr, Fe–10Cr, Fe–18Cr and Fe–25Cr) in O2 and in O2 + H2O environment at 600 °C, Oxid. Met. 75 (2011) 183–207, https://doi.org/10.1007/s11085-010-9229-z.
[40] J. Eklund, I. Hanif, S. Bigdeli, T. Jonsson, High temperature corrosion behavior of FeCrAlSi model alloys in the presence of water vapor and KCl at 600 °C – the influence of Cr content, Corros. Sci. 198 (2022), 110114, https://doi.org/10.1016/j.corsci.2022.110114.
[41] H.J. Grabke, E. Reese, M. Spiegel, The Effects of Chlorides, Hydrogen Chloride, and Sulfur Dioxide in the Oxidation of Steels below Deposits, 1995.
[42] L. Reddy, M. Sattari, C.J. Davis, P.H. Shipway, M. Halvarsson, T. Hussain, Influence of KCl and HCl on a laser clad FeCrAl alloy: In-Situ SEM and controlled environment high temperature corrosion, Corros. Sci. 158 (2019), 108076, https://doi.org/10.1016/J.CORSCI.2019.07.003.
[43] B. Liu, X. Chen, Impacts of temperature and KCl on corrosion behavior of 12Cr1MoVG and T91 in HCl-containing atmosphere, Oxid. Met. 90 (2018) 585–597, https://doi.org/10.1007/s11085-018-9864-3.
[44] J. Töpfer, S. Aggarwal, R. Dieckmann, Point defects and cation tracer diffusion in (CrxFe1 − x)3 − δO4 spinels, Solid State Ion. 81 (1995) 251–266, https://doi.org/10.1016/0167-2738(95)00190-H.
[45] T. Jonsson, B. Pujilaksono, H. Heidari, F. Liu, J.-E. Svensson, M. Halvarsson, L.-G. Johansson, Oxidation of Fe–10Cr in O2 and in O2+H2O environment at 600°C: a microstructural investigation, Corros. Sci. 75 (2013) 326–336, https://doi.org/10.1016/j.corsci.2013.06.016.
[46] T. Jonsson, H. Larsson, S. Karlsson, H. Hooshyar, M. Sattari, J. Liske, J.-E. Svensson, L.-G. Johansson, High-temperature oxidation of FeCr(Ni) alloys: the behaviour after breakaway, Oxid. Met. 87 (2017) 333–341, https://doi.org/10.1007/s11085-017-9731-7.
[47] S. Kiamehr, K.V. Dahl, M. Montgomery, M.A.J. Somers, KCl-induced high temperature corrosion of selected commercial alloys, Mater. Corros. 66 (2015) 1414–1429, https://doi.org/10.1002/maco.201408213.
[48] H. Larsson, T. Jonsson, R. Naraghi, Y. Gong, R.C. Reed, J. Ågren, Oxidation of iron at 600 °C – experiments and simulations, Mater. Corros. 68 (2017) 133–142, https://doi.org/10.1002/maco.201508781.
[49] M.J. Graham, D. Caplan, R.J. Hussey, The effect of oxide grain structure on the high-temperature oxidation of Fe, Ni and Cr, Can. Metall. Q. 18 (1979) 283–291, https://doi.org/10.1179/cmq.1979.18.3.283.
[50] L. Bataillou, C. Desgranges, L. Martinelli, D. Monceau, Modelling of the effect of grain boundary diffusion on the oxidation of Ni-Cr alloys at high temperature, Corros. Sci. 136 (2018) 148–160, https://doi.org/10.1016/J.CORSCI.2018.03.001.
[51] A. Atkinson, R.I. Taylor, A.E. Hughes, A quantitative demonstration of the grain boundary diffusion mechanism for the oxidation of metals, Philos. Mag. A 45 (1982) 823–833, https://doi.org/10.1080/01418618208239905.
[52] W.H. Bragg, XXX. The structure of the spinel group of crystals, Lond. Edinb. Dublin Philos. Mag. J. Sci. 30 (1915) 305–315, https://doi.org/10.1080/14786440808635400.
[53] X. Liang, Y. Zhong, S. Zhu, H. He, P. Yuan, J. Zhu, Z. Jiang, The valence and site occupancy of substituting metals in magnetite spinel structure Fe3−xMxO4 (M = Cr, Mn, Co and Ni) and their influence on thermal stability: An XANES and TG-DSC investigation, Solid State Sci. 15 (2013) 115–122, https://doi.org/10.1016/j.solidstatesciences.2012.10.005.
[54] A. Zahs, M. Spiegel, H. Grabke, The influence of alloying elements on the chlorine-induced high temperature corrosion of Fe-Cr alloys in oxidizing atmospheres, Mater. Corros. 50 (1999) 561–578, https://doi.org/https://doi.org/10.1002/(SICI)1521-4176(199910)50:10<561::AID-MACO561>3.0.CO;2-L.
[55] Y. Kawahara, High temperature corrosion mechanisms and effect of alloying elements for materials used in waste incineration environment, Corros. Sci. 44 (2002) 223–245, https://doi.org/10.1016/S0010-938X(01)00058-0.
[56] J. Eklund, A. Persdotter, V. Ssenteza, T. Jonsson, The long-term corrosion behavior of FeCrAl(Si) alloys after breakaway oxidation at 600 °C, Corros. Sci. 217 (2023), 111155, https://doi.org/10.1016/j.corsci.2023.111155.
[57] T. Sand, S. Bigdeli, M. Sattari, J. Andersson, M. Hättestrand, T. Helander, J. Eklund, J.-E. Svensson, M. Halvarsson, L.-G. Johansson, Efficacy of an external chromia layer in reducing nitridation of high temperature alloys, Corros. Sci. 197 (2022), 110050, https://doi.org/10.1016/j.corsci.2021.110050.
[58] N. Israelsson, K.A. Unocic, K. Hellström, T. Jonsson, M. Norell, J.-E. Svensson, L.-G. Johansson, A microstructural and kinetic investigation of the KCl-induced corrosion of an FeCrAl alloy at 600 °C, Oxid. Met. 84 (2015) 105–127, https://doi.org/10.1007/s11085-015-9546-3.

[59] N. Mortazavi, L. Intiso, N. Israelsson, L.-G. Johansson, M. Halvarsson, In situ ESEM investigation of KCl-induced corrosion of a FeCrAl and a model FeNiCrAl alloy in lab air at 450°C, J. Electrochem Soc. 162 (2015) C744–C753, https://doi.org/10.1149/2.0581514jes.
[60] N. Israelsson, K.A. Unocic, K. Hellström, J.-E. Svensson, L.-G. Johansson, Cyclic corrosion and chlorination of an FeCrAl alloy in the presence of KCl, Oxid. Met. 84 (2015) 269–290, https://doi.org/10.1007/s11085-015-9554-3.
[61] J.J. Barnes, G.Y. Lai, Factors affecting the nitridation behavior of Fe-base, Ni-base, and Co-base alloys in pure nitrogen, Le. J. De. Phys. IV 03 (C9) (1993) 167–C9-174, https://doi.org/10.1051/jp4:1993915.
[62] F.G. Wilson, T. Gladman, Aluminium nitride in steel, Int. Mater. Rev. 33 (1988) 221–286, https://doi.org/10.1179/imr.1988.33.1.221.
[63] X. Peng, J. Yan, Y. Zhou, F. Wang, Effect of grain refinement on the resistance of 304 stainless steel to breakaway oxidation in wet air, Acta Mater. 53 (2005) 5079–5088, https://doi.org/10.1016/J.ACTAMAT.2005.07.019.
[64] V. Trindade, H.-J. Christ, U. Krupp, Grain-size effects on the high-temperature oxidation behaviour of chromium steels, Oxid. Met. 73 (2010) 551–563, https://doi.org/10.1007/s11085-010-9192-8.
[65] V.B. Trindade, U. Krupp, B.Z. Hanjari, S. Yang, H.-J. Christ, Effect of alloy grain size on the high-temperature oxidation behavior of the austenitic steel TP 347, Mater. Res. 8 (2005) 371–375, https://doi.org/10.1590/S1516-14392005000400003.
[66] S.N. Basu, G.J. Yurek, Effect of alloy grain size and silicon content on the oxidation of austenitic Fe-Cr-Ni-Mn-Si alloys in pure O2, Oxid. Met. 36 (1991) 281–315, https://doi.org/10.1007/BF00662967.
[67] C. Pettersson, T. Jonsson, C. Proff, M. Halvarsson, J.-E. Svensson, L.-G. Johansson, High temperature oxidation of the austenitic (35Fe27Cr31Ni) alloy Sanicro 28 in O2 + H2O environment, Oxid. Met. 74 (2010) 93–111, https://doi.org/10.1007/s11085-010-9199-1.
[68] C. Desgranges, F. Lequien, E. Aublant, M. Nastar, D. Monceau, Depletion and voids formation in the substrate during high temperature oxidation of Ni–Cr alloys, Oxid. Met. 79 (2013) 93–105, https://doi.org/10.1007/s11085-012-9328-0.